

# SUPPLEMENTARY INFORMATION

## Mechanism of amorphous phase stabilization in ultrathin films of monoatomic phase change material

Daniele Dragoni,<sup>†</sup> Jörg Behler,<sup>‡</sup> and Marco Bernasconi<sup>\*,¶</sup>

<sup>†</sup>*Department of Materials Science, University of Milano-Bicocca, Via R. Cozzi 55, Milano,  
Italy*

<sup>‡</sup>*Institut für Physikalische Chemie, Theoretische Chemie, Universität Göttingen,  
Tammannstr. 6, 37077 Göttingen, Germany*

<sup>¶</sup>*Dipartimento di Scienza dei Materiali, Università di Milano-Bicocca, Via R. Cozzi 55,  
I-20125 Milano, Italy*

E-mail: marco.bernasconi@unimib.it

We provide supplementary information on the results concerning the generation of the Neural Network potential and on the simulation of the crystallization of Sb in bulk and in the thin film.

**Neural Network potential training and testing.** The Neural Network (NN) potential was generated by fitting a training set consisting of the DFT energy and forces of 19851 configurations (1909188 local atomic environments) of crystalline, liquid and amorphous models containing from 54 to 144 atoms at different temperatures and densities. The test set consisted instead of about 3228 configurations (313704 local atomic environments). The root mean square error (RMSE) on the energy and forces of training (test) sets are 6.04 (7.07) meV/atom and 0.18 (0.20) eV/Å respectively (see Fig. S1).

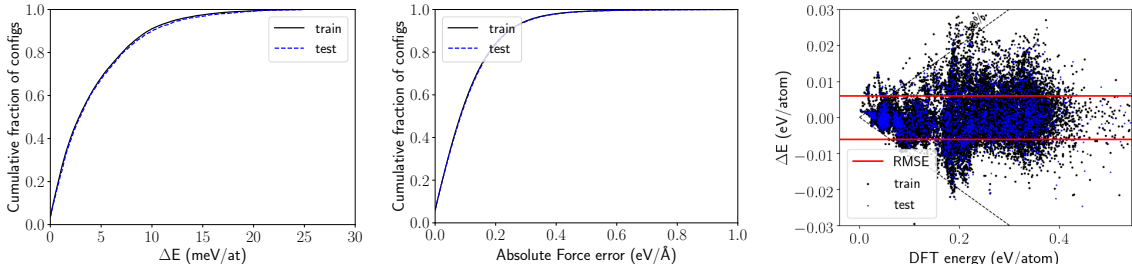


**Figure S1:** Cumulative fraction of configurations as a function of the absolute error in (left panel) energy (per atom) and (central panel) forces. Training and test curves are reported for clarity. (Right panel) Distribution of absolute error as a function of the reference energy of configurations included in the training set (black dots) and test set (blue dots). The RMSE of the training (test) set are 6.04 (7.07) meV/atom on the energy and 0.18 (0.20) eV/Å on the forces.

The potential is devised to describe Sb in different phases at very different conditions of temperature and pressure. To reach this goal within our implementation of the NN scheme, it is necessary to include in the training set also configurations very far from those that are actually explored in the MD simulations at the conditions of interest. This is needed to train the potential to avoid unphysical region of the phase space. The energy and forces for these configurations are very high. The RMSE in the energy and forces is particularly high for these high energy configurations which, however, does not affect the quality of the potential

in reproducing the phase space of interest as it is shown by the validation on the structural and dynamical properties reported below.

The NN potential was validated by comparing the structural properties of the crystal, liquid and amorphous phases with DFT results obtained within the same framework (PBE functional,<sup>1</sup> norm conserving pseudopotentials and plane wave expansion of Kohn-Sham orbitals) used to generate the fitting database. The structural parameters of the trigonal crystalline phase obtained with the NN potential or with the NN potential supplemented by the semiempirical van der Waals interaction due to Grimme (D2)<sup>2</sup> are compared with DFT-PBE and DFT-PBE+D2 results obtained with the Quantum-Espresso (QE) code<sup>3</sup> and the same setting used for the generation of the fitting database (see Computational Details in the article). Antimony crystallizes in the A7 structure ( $R\bar{3}m$  space group) that can be described by a rhombohedral unit cell with two atoms or by a conventional hexagonal cell with six atoms stacked in the ABCABC sequence.<sup>4</sup> The structure consists of puckled bilayers perpendicular to the [111] direction, with strong and short intrabilayer bonds and weaker and long interbilayer bonds (see Table S1).

**Table S1: Structural parameters (hexagonal setting), bulk modulus and equilibrium volume per atom of the A7 trigonal crystalline phase<sup>4</sup> computed within the NN or NN+D2 potentials compared with DFT-PBE, DFT-PBE+D2 results and with experimental structural data from Ref. 4. The experimental bulk modulus is taken from Ref. 5. The lengths of the short  $r_s$  and long  $r_l$  bonds in the A7 phase are also reported.**

	NN	NN+D2	DFT-PBE	DFT-PBE+D2	Expt.
$a$ [Å]	4.361	4.243	4.36	4.29	4.3007
$c$ [Å]	11.496	11.377	11.39	10.96	11.222
$V_0$ [Å <sup>3</sup> ]	31.562	29.571	31.33	29.06	29.959
B [GPa]	33.68	44.29	36.0		38.3
$r_s$ [Å]	2.95	2.93	2.95	2.92	2.902
$r_l$ [Å]	3.41	3.28	3.39	3.25	3.343

The pair correlation function, the distribution of the coordination numbers and the bond angle distributions obtained from NN and NN+D2 simulations are compared with DFT-PBE and DFT-PBE+D2 results from QE simulations for liquid Sb at 1000 K in Figs. S2-S4.

Experimental data<sup>6</sup> for the pair correlation function at 973 K are also shown in Fig. S2.

The cubic simulation cell contains 1152 atoms in NN+D2 simulations and 144 atoms in DFT simulations. The pair correlation function, the distribution of the coordination numbers and the bond angle distributions of amorphous Sb at 300 K, computed within NN, NN-D2, DFT-PBE, DFT-PBE+D2 frameworks are compared in Figs. S5-S7. Structural properties for the liquid and the amorphous models are averaged over NVT run 100 ps long. The density of both liquid and amorphous models is set to the experimental density of the liquid at melting ( $0.0320 \text{ atom}/\text{\AA}^3$ )<sup>7</sup> which is essentially equal to the theoretical equilibrium density at melting ( $0.0319 \text{ atom}/\text{\AA}^3$ , see article). The agreement between NN/NN+D2 and DFT-PBE/DFT-PBE+D2 results is excellent for crystalline, liquid and amorphous phases which validates the quality of the NN potential. Similarly, good agreement between NN and DFT results is also found for the liquid and amorphous phases at densities far from the equilibrium density corresponding to either -10 % or +15 % of the equilibrium density. The structural properties reported in Figs. S5-S7 are very similar with previous DFT results from Refs. 8–11.

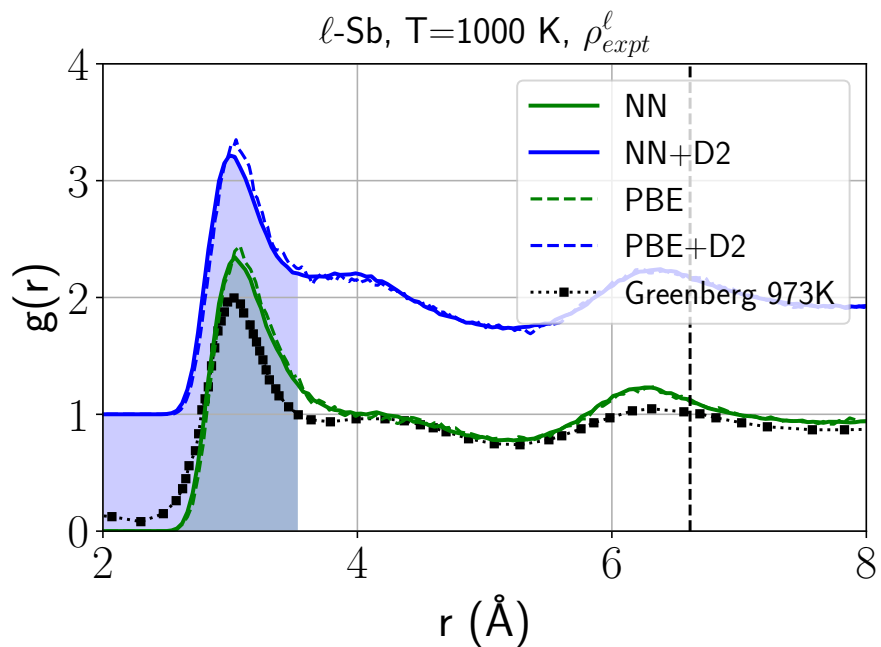


**Figure S2:** Pair correlation function of liquid Sb at 1000 K at the experimental density of the liquid at melting (see article) from NVT simulations with the Neural Network potential (NN, green line) or the NN potential supplemented by the Grimme (D2) van der Waals interaction (NN+D2, blue line), compared with the results from DFT molecular dynamics with the PBE functional (PBE, green dashed line) or PBE+D2 (blue dashed line). Experimental data at 973 K (black squares) are taken from Greenberg et al.<sup>6</sup> The dashed area define the bonding cutoff of 3.66 Å used to compute coordination numbers and other observables. A cubic 144-atom (1152-atom) supercell was used for DFT (NN) simulations. The vertical dashed line indicates the cutoff used in the symmetry functions for the generation of the NN potential.

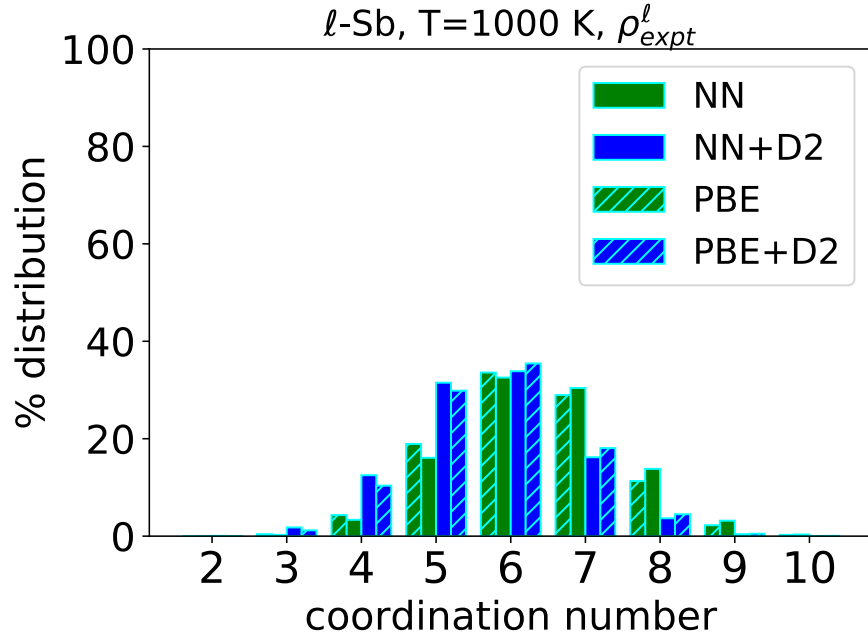


**Figure S3:** Distribution of coordination numbers of liquid Sb at 1000 K from NN, NN+D2 and DFT-PBE or DFT-PBE+D2 simulations at the experimental density of the liquid at melting obtained by integrating the pair correlation functions of Fig. S2 up to the bonding cutoff of 3.66 Å.

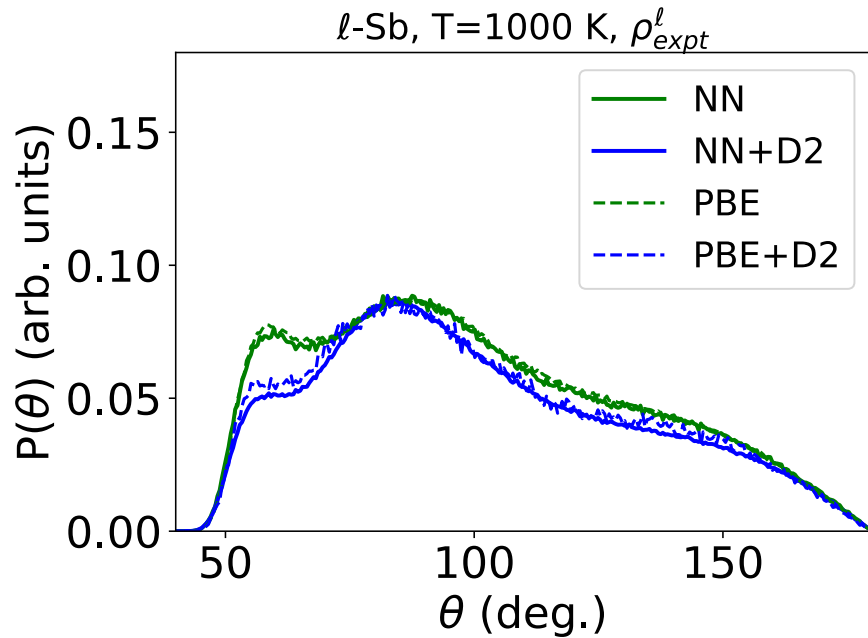


**Figure S4:** Bond angle distributions of liquid Sb at 1000 K from NN, NN+D2 and DFT-PBE or DFT-PBE+D2 simulations at the experimental density of the liquid at melting. The bonding cutoff of 3.66 Å was used.

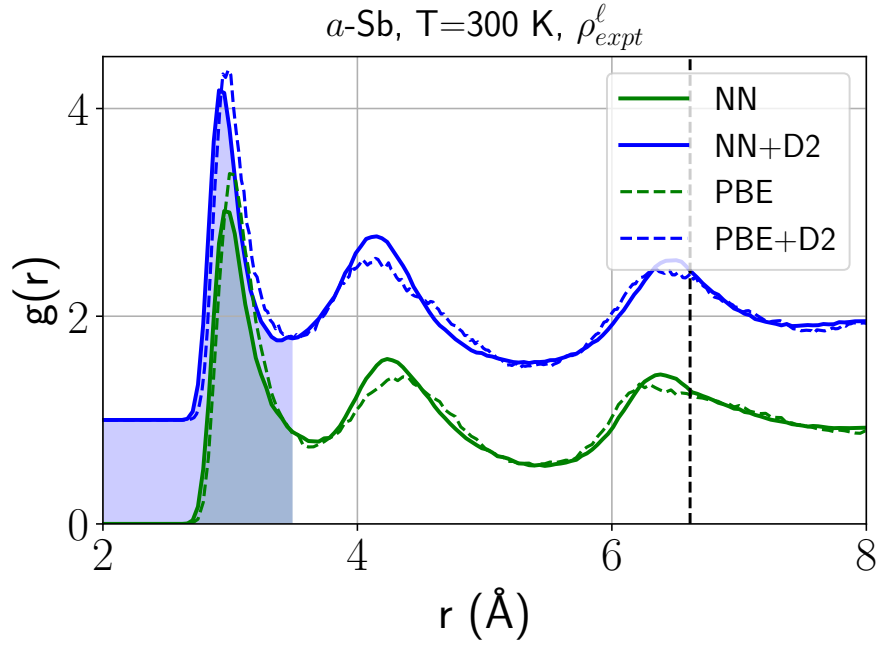


**Figure S5:** Pair correlation function of amorphous Sb at 300 K from NN, NN+D2 and DFT-PBE or DFT-PB+D2 simulations. All the amorphous models were generated by quenching from 1000 K to 300 K in 80 ps with the density fixed at the experimental value of the liquid at melting (see article). The dashed area defines the bonding cutoff of 3.5  $\text{\AA}$  also used in Ref. 8. The vertical dashed line indicates the cutoff used in the symmetry functions for the generation of the NN potential.

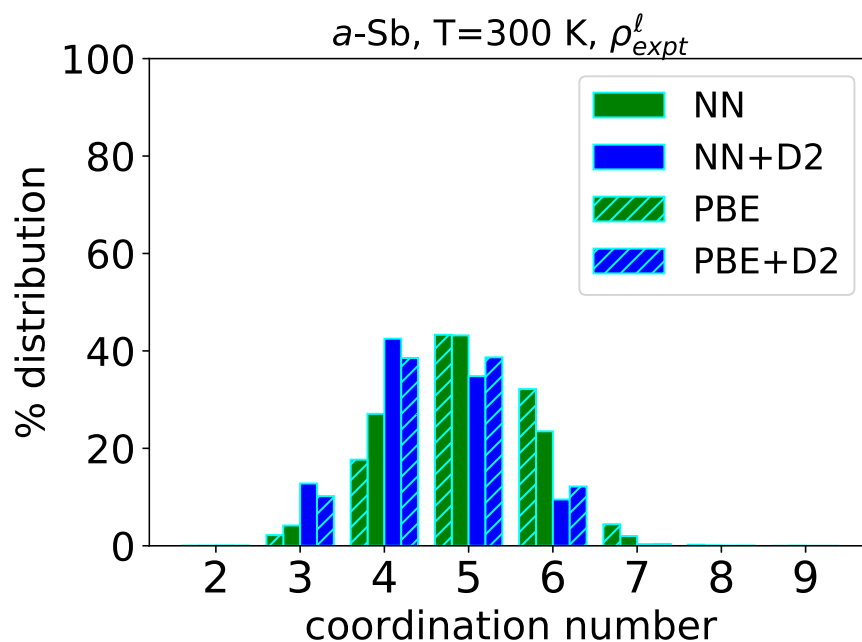


**Figure S6:** Distribution of coordination numbers of amorphous Sb at 300 K from NN, NN+D2 and DFT-PBE or DFT-PBE+D2 simulations at the experimental density of the liquid at melting. The bonding cutoff of 3.5 Å was used.

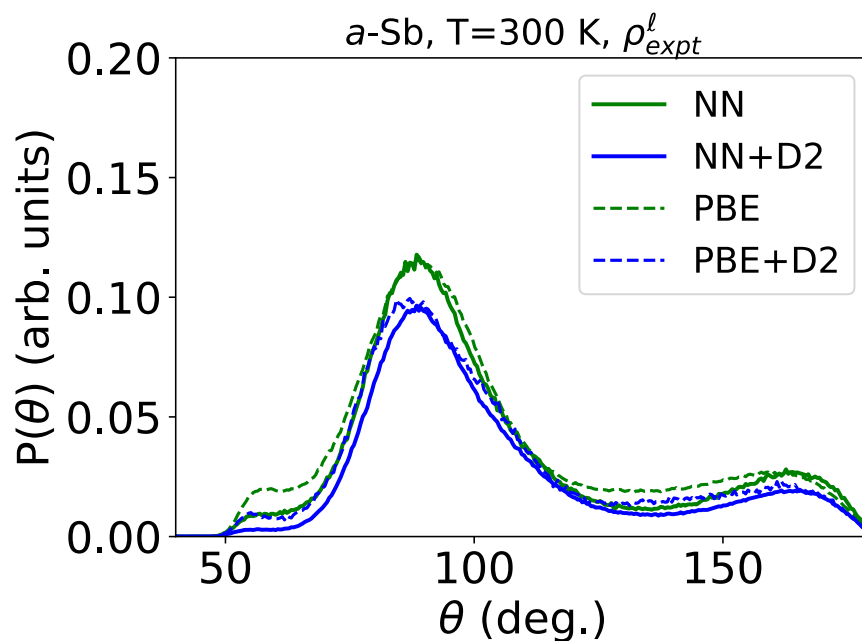


**Figure S7:** Bond angle distributions of amorphous Sb at 300 K from NN, NN+D2 and DFT-PBE or DFT-PBE+D2 simulations at the experimental density of the liquid at melting. The bonding cutoff of 3.5 Å was used.



**Order parameter.** In order to assess whether an atom  $i$  belongs to the crystal or the liquid/amorphous phase, we have employed the averaged local order parameter  $\bar{q}_{4m}(i)$  described in Ref. 12 to build an order parameter  $\bar{Q}_4(i)$  as

$$\begin{aligned}
\bar{Q}_4(i) &= \frac{1}{N_b(i)} \sum_{j=1}^{N_b(i)} \frac{\sum_{m=-4}^4 \bar{q}_{4m}(i) \bar{q}_{4m}(j)^*}{(\sum_{m=-4}^4 |\bar{q}_{4m}(i)|^2)^{1/2} (\sum_{m=-4}^4 |\bar{q}_{4m}(j)|^2)^{1/2}} \\
\bar{q}_{4m}(i) &= \frac{1}{\hat{N}_b(i)} \sum_{k=0}^{\hat{N}_b(i)} q_{4m}(k) \\
q_{4m}(k) &= \frac{1}{N_b(k)} \sum_{l=1}^{N_b(k)} Y_{4m}(\hat{\mathbf{r}}_{kl})
\end{aligned} \tag{1}$$

where  $j$  runs over the  $N_b(i)$  neighboring atoms,  $k$  runs over the  $\hat{N}_b(i)$  neighboring atoms including the  $i$ -th atoms itself, and  $Y_{4m}(\hat{\mathbf{r}}_{kl})$  are the spherical harmonics of the polar angles defined by the versor  $\hat{\mathbf{r}}_{kl}$  which links atoms  $i$  and  $j$ . The neighboring  $N_b(i)$  atoms include the first coordination shell of crystalline Sb at its theoretical equilibrium density. We define as crystalline an atom with  $\bar{Q}_4$  greater than 0.8 (Fig. S8), and we consider two crystalline atoms as connected up to a cutoff distance of 3.6 Å.

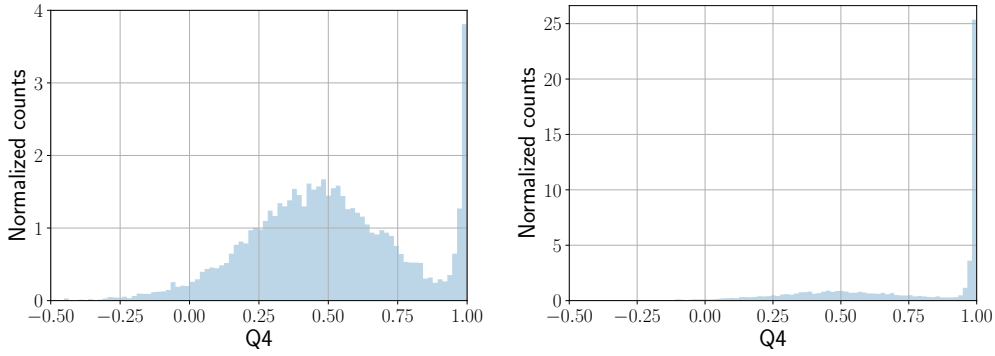


**Figure S8:** Normalized distribution of  $\bar{Q}_4$  calculated for all atoms in bulk at 300 K during the growth of a crystalline front. Initial and intermediate steps are shown in the left and right panels respectively.

**Simulation of crystallization in bulk and in the thin film.** The  $\bar{Q}_4$  parameter is used to identify the position of the crystalline front as defined in the article. The displacement of the crystal growth front as a function of time is shown in Fig. S9 for the simulation (NN+D2) in the bulk at different temperatures at the experimental density of the liquid at melting. Snapshots of the evolution in time of supercritical nuclei in the bulk at 600 K are shown in Fig. S10.

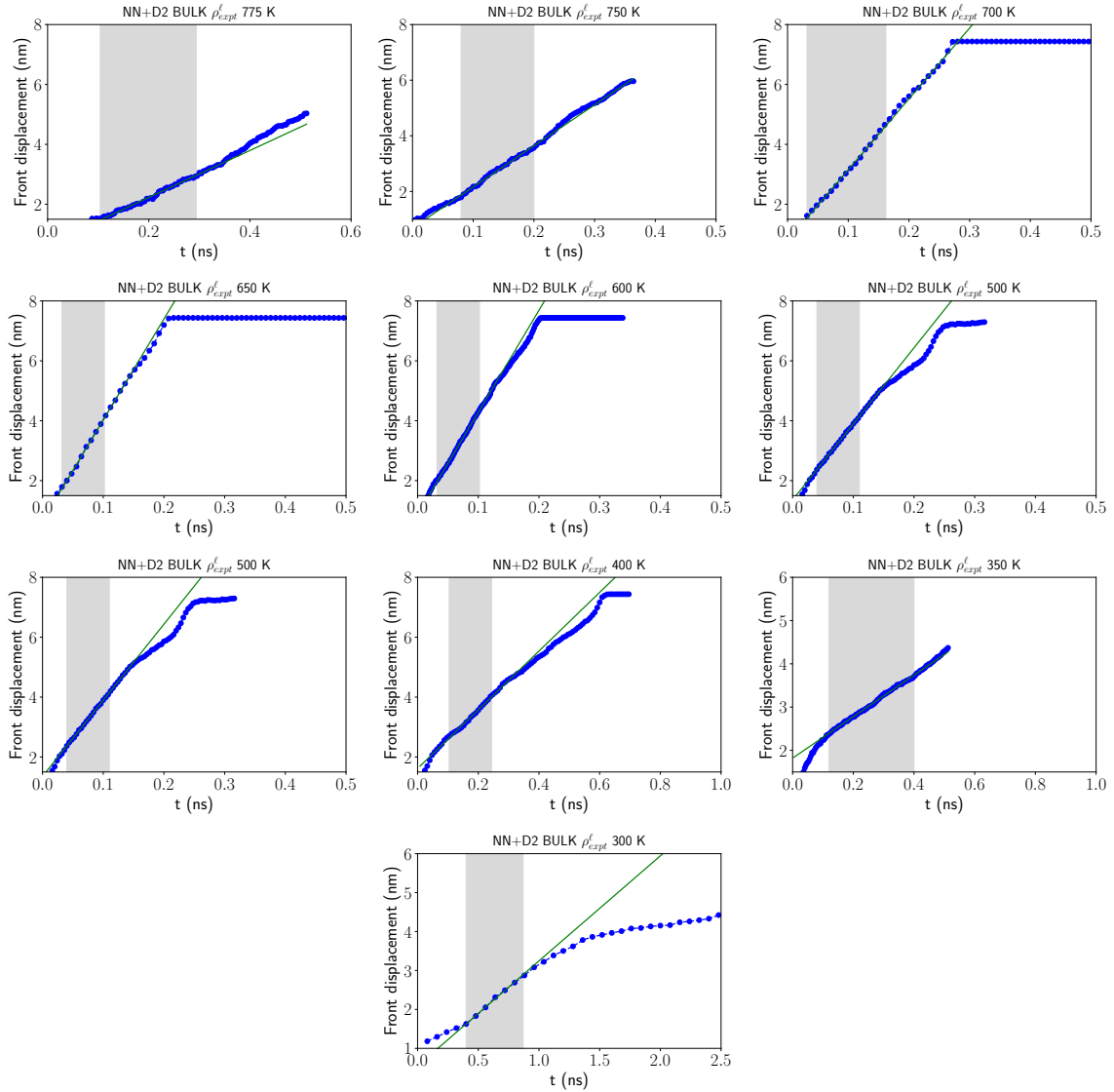


**Figure S9:** Displacement of the crystal growth front ( $L_{cr}(t) - L_{cr}(0)$ , see main text) as a function of time in the simulation of the crystallization in the bulk at different temperatures. The shaded area corresponds to the time lag used to fit the data with a linear function to extract the crystal growth velocity.

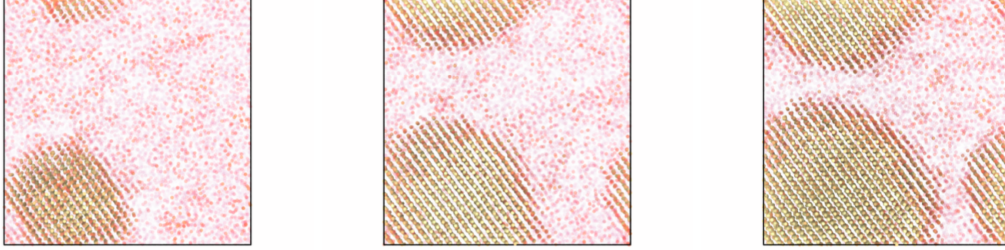


**Figure S10:** Evolution in time of supercritical nuclei in the simulation of the crystallization in the bulk at 600 K. Snapshots are taken at 0 ps (left), 35 ps (central) and 60 ps (right). Transparency is assigned by the value of the order parameter for crystallinity to highlight the presence of crystallites.

The alternation of short and long bonds typical of the A7 crystalline geometry survives in the amorphous phase although in a disordered manner. This feature is highlighted by the angular-limited bond correlation (ALTBC) function<sup>13</sup> which measures the probability of finding a bond with length  $r_1$  mostly aligned (within a threshold angle of  $25^\circ$ ) with a second bond of length  $r_2$  formed with the same central atom. The ALTBC function for a-Sb at 300 K reported in Fig. S11 shows indeed two features due to the alternation of short and long bonds as also reported in previous DFT works on a-Sb.<sup>8</sup> Our a-Sb model was generated by quenching from 1000 to 300 K in 80 ps and it was then equilibrated at room temperature for 120 ps. The ALTBC of the amorphous phase has to be compared with that of the recrystallized model shown in Fig. S11. The bimodal distribution is strongly enhanced in the recrystallized phase. However, a third feature appears along the diagonal which corresponds to two bonds with nearly equal length and nearly aligned along the same direction. This feature arises from defective structure in the recrystallized phase. Finally, Fig. S12 reports the mean square displacement as a function of time of a-Sb heated at different temperatures while Fig. S13 reports the displacement of the crystalline front as a function of time and at different temperatures in the film.

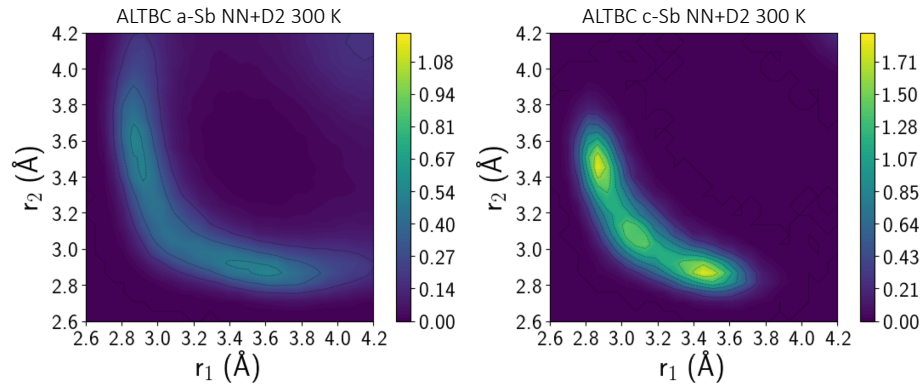


**Figure S11:** Angular-limited bond correlation (ALTBC) function for the NN+D2 model of (left panel) a-Sb at 300 K and of (right panel) the recrystallized model at the same temperature. The density is fixed at the equilibrium density of the liquid at melting. Radial distances  $r_1$  and  $r_2$  are in Å.

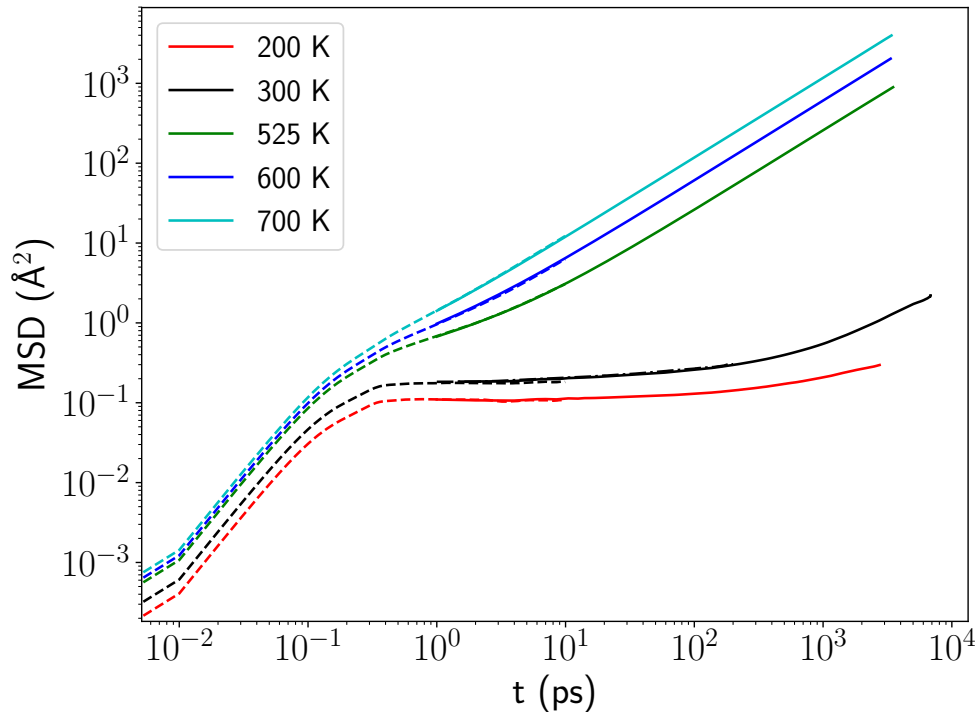


**Figure S 12:** Mean square displacement (MSD) of the model of bulk a-Sb at different temperatures computed from NVT simulations. Dashed lines are short simulations (up to 10 ps) with data collected every 10 fs. Solid lines are longer simulations with data collected every 1 ps. The raising of the MSD at long times after the plateau at 300 K is typical of the  $\alpha$  relaxation in a supercooled liquid above the glass transition, while the same feature at 200 K is consistent with the aging of the amorphous model quenched in about 80 ps from the melt.

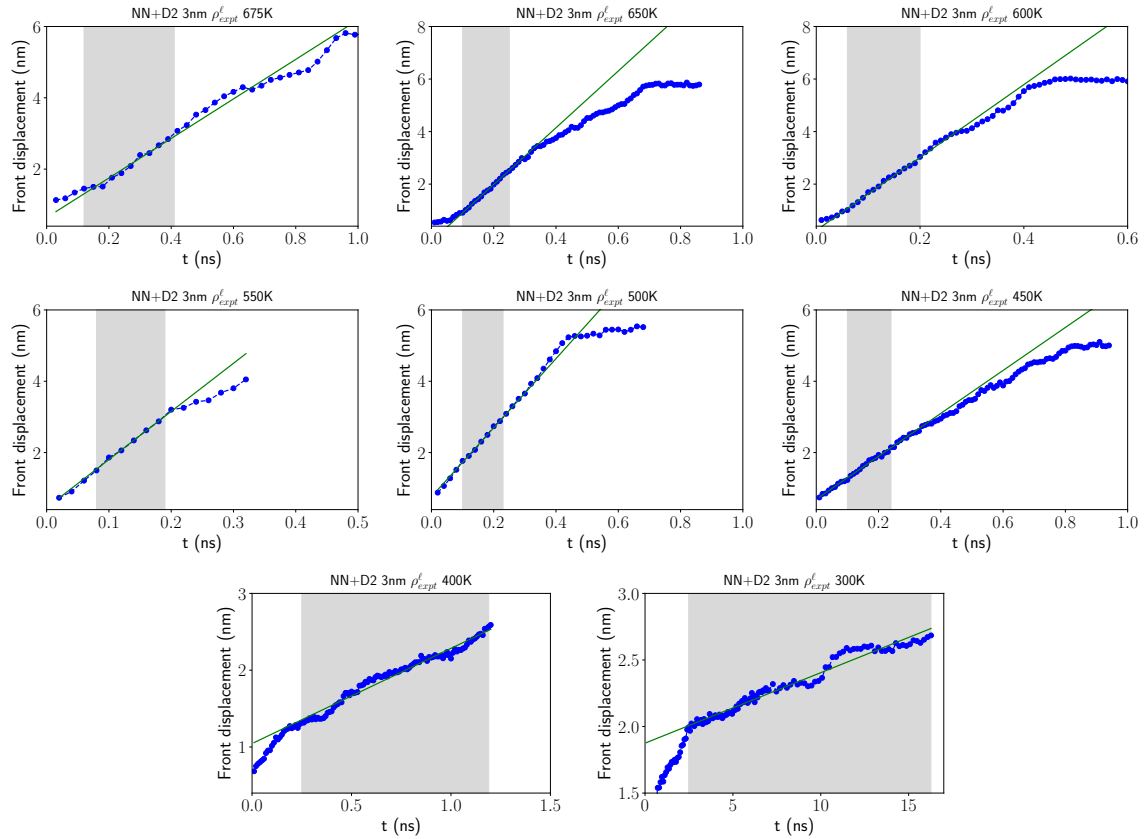


**Figure S13:** Displacement of the crystal growth front ( $L_{cr}(t) - L_{cr}(0)$ , see main text) as a function of time in the simulation of the crystallization in the 3 nm film at different temperatures. The shaded area corresponds to the time lag used to fit the data with a linear function to extract the crystal growth velocity.

## References

- (1) J. P. Perdew, K. Burke, and M. Ernzerhof, Generalized Gradient Approximation Made Simple. *Phys. Rev. Lett.* 1996, **77**, 3865.
- (2) S. Grimme, Semiempirical GGA-type Density Functional Constructed with a Long-Range Dispersion Correction. *J. Comp. Chem.* 2006, **27**, 1787-1799.
- (3) P. Giannozzi, *et al.*, QUANTUM ESPRESSO: a Modular and Open-Source Software Project for Quantum Simulations of Materials. *J. Phys.: Condensed Matter* 2009, **21**, 395502.
- (4) C. Barrett, P. Cucka, and K. Haefner, The Crystal Structure of Antimony at 4.2, 78 and 298 K. *Acta Crystall.* 1963, **16**, 451-453.
- (5) Kittel, C. *Introduction to Solid State Physics*, Wiley, 8<sup>th</sup> edition, pag. 52, 2004.
- (6) Y. Greenberg, E. Yahel, E. N. Caspi, B. Beuneu, M. P. Dariel, and G. Makov, On the Relation Between the Microscopic Structure and the Sound Velocity Anomaly in Elemental Melts of Groups IV, V, and VI. *J. Chem. Phys.* 2010, **133**, 094506.
- (7) A. Crawley and D. Kiff, The Density and Viscosity of Liquid Antimony. *Metall. Mater. Transact. B* 1972, **3**, 157-159.
- (8) I. Ronneberger, Y. Chen, W. Zhang, and R. Mazzarello, Local Structural Origin of the Crystallization Tendency of Pure and Alloyed Sb. *Phys. Status Solidi (RRL)* 2019, **13**, 1800552; I. Ronneberger, Dr. rer. nat. thesis, RWTH Aachen University, 2016.
- (9) M. Salinga, B. Kersting, I. Ronneberger, V. P. Jonnalagadda, X. T. Vu, M. Le Gallo, I. Giannopoulos, O. Cojocar-Mirédin, R. Mazzarello, and A. Sebastian, Monatomic Phase Change Memory. *Nat. Mater.* 2018, **17**, 681-685.
- (10) M. Ropo, J. Akola, and R. O. Jones, Crystallization of Supercooled Liquid Antimony: a Density Functional Study. *Phys. Rev. B* 2017, **96**, 184102.

- (11) Y. Sun, C. Yu, X. Zhu, H. Zou, Y. Hu, M. Pei, L. Zhai, Y. Sui, W. Wu, Z. Song, Insight Into the Role of Nitrogen in the Phase-Change Material Sb. *J. Phys. D: Appl. Phys.* **2019**, *52*, 455107.
  
- (12) W. Lechner, and C. Dellago, Accurate Determination of Crystal Structures Based on Averaged Local Bond Order Parameters. *J. Chem. Phys.* 2008, **129**, 114707.
  
- (13) C. Bichara, A. Pellegatti, and J.-P. Gaspard, Properties of Liquid Group-V Elements: a Numerical Tight-Binding Simulation. *Phys. Rev. B* 1993, **47**, 5002.